MATERIALS CHEMISTRY FRONTIERS

CHINESE CHEMICAL SOCIETY

ROYAL SOCIETY OF CHEMISTRY

RESEARCH ARTICLE

View Article Online
View Journal | View Issue

Check for updates

Cite this: *Mater. Chem. Front.*, 2023, **7**, 4109

PVP-coated ultrasmall Nd-doped Gd_2O_2S nanoparticles for multimodal imaging†

Qilin Zou,[ab] Luan Passini,[b] Laure Gibot,[b] Delphine Lagarde,[c] Jie Hu,[d] Haomiao Zhu,[d] Franck Desmoulin,[e] Pierre Sicard,[f] Nitchawat Paiyabhroma,[f] Marc Verelst,[a] Robert Mauricot*[a] and Clément Roux *[b]

Received 12th May 2023,
Accepted 20th June 2023

DOI: 10.1039/d3qm00554b

rsc.li/frontiers-materials

Rare-earth (RE) based inorganic nanoparticles (NPs) are emerging nanoprobes, which have been widely explored. Single RENPs as a contrast agent for multimodal bioimaging possess the ability to combine optical, ultrasonic, magnetic and electronic properties without signal interference. In this study, we present a versatile strategy for the synthesis of 15 kinds of ultrasmall rare-earth oxysulfide (RE_2O_2S) NPs with a size of 3–10 nm. PVP-coated $Gd_{0.8}Nd_{1.2}O_2S$ NPs with a size of 6 nm are synthesized through a ligand exchange method and their colloidal stability in culture medium is studied. We demonstrate that the as-prepared NPs are capable of being employed in both T_1- and T_2-weighted magnetic resonance, X-ray computed tomography, photoacoustic, ultrasound, and second near infrared fluorescence imaging. The results pave the way for bioapplications of ultrasmall RE_2O_2S NPs.

Open Access Article. Published on 03 2023. Downloaded on 8/25/2025 2:35:29 AM.
This article is licensed under a Creative Commons Attribution-NonCommercial 3.0 Unported Licence.

Introduction

In recent decades, biomedical imaging technologies have been exploited for early disease detection and diagnosis. Several imaging modes such as computed tomography (CT), magnetic resonance imaging (MRI), photoacoustic imaging (PAI), positron-emission tomography (PET), single-photon-emission computed tomography (SPECT), and optical imaging (OI) play important roles in the observation of the structures and functions of biological systems, and provide important information concerning the pathogenesis, progression and treatment of diseases such as cancer.[1,2] Using a monomodal imaging technique usually cannot meet the requirements of high sensitivity and spatial resolution because of their respective drawbacks. Consequently, the combination of two or more than two imaging modalities, so called dual- or multi-modal imaging, is a popular way to overcome these limitations.[3,4] Nowadays, combining various components into one platform is the most commonly used strategy to take advantage of their respective functions. This strategy is impeded by the complicated composition and synthetic procedure, inevitable interference, poor reproducibility and uncertain pharmacokinetics, and hence less accessible for clinical use. Alternatively, one component with multiple contrasting capacities remains more desirable due to the lower interference, simpler fabrication, defined structures, and far better reproducibility than the composite agents.

Thanks to the development of instruments, OI in the second near-infrared (NIR-II) biological window (1000–1700 nm) has attracted much attention because of deep tissue penetration, low light scattering and autofluorescence interference.[5–8] At present, many probes, such as small organic molecule dyes, inorganic quantum dots (QDs), and single-walled carbon nanotubes (SWCNTs), are able to generate NIR-II fluorescence. Among them, rare earth doped nanoparticles (RENPs) have demonstrated great contrasting powers for NIR-II bioimaging because of their excellent optical performance such as large anti-Stokes or Stokes shift, sharp emission profiles, long lifetime, low biotoxicity, and low background autofluorescence during their detection.[4,9] Generally, Yb^{3+} or Nd^{3+} ions are singly- or co-doped in RENPs to absorb 980 nm or 800 nm NIR excitation photons ($^2F_{7/2} \rightarrow {}^2F_{5/2}$ transition of Yb^{3+} ions, $^4I_{9/2} \rightarrow {}^4F_{5/2}$ transition of Nd^{3+} ions), where low-cost, high-power diode lasers are commercially available, which makes RENPs more suitable for bioimaging. Besides, compared to

[a] *Centre d'Elaboration des Matériaux et d'Etudes Structurales, CNRS, Université de Toulouse-UPS, France*
[b] *Laboratoire des IMRCP, CNRS UMR 5623, Université de Toulouse-UPS, France. E-mail: clement.roux1@univ-tlse3.fr*
[c] *LPCNO, Université de Toulouse, INSA-CNRS-UPS, France*
[d] *CAS Key Laboratory of Design and Assembly of Functional Nanostructures, Fujian Key Laboratory of Nanomaterials, Fujian Institute of Research on the Structure of Matter, Chinese Academy of Sciences, China*
[e] *ToNIC, Toulouse NeuroImaging Center, CREFRE, Université de Toulouse, Inserm, UPS, France*
[f] *IPAM/PhyMedExp/Biocampus, INSERM, CNRS, Université de Montpellier, France*

† Electronic supplementary information (ESI) available: Method description for US and PA imaging, and MRI and relaxivity; size summarization; TEM images; XRD patterns; DLS, magnetization curves and T_1 and T_2 relaxivity plots at 7 T of the nanoparticles synthesized under different conditions, absorbance and PA_{exc} spectrum. See DOI: https://doi.org/10.1039/d3qm00554b

Open Access Article. Published on 03 2023. Downloaded on 8/25/2025 2:35:29 AM. This article is licensed under a Creative Commons Attribution-NonCommercial 3.0 Unported Licence.

fluorescence produced by radiative transitions, the PA signal is produced by nonradiative decay pathways from the excited state to the ground state, after absorbing NIR photons. PAI is an emerging non-invasive imaging tool that can provide large penetration depth beyond the optical diffusion limit while maintaining high spatial resolution but the sensitivity is not always satisfactory. In the same way, ultrasound imaging (USI), also called echography, often coupled with PAI devices, also allows extracting deep body molecular imaging data by recording specific echo reflection of pulsed ultrasonic waves using an endogenous contrast agent like hemoglobin.[10]

For complimentary but non-optical imaging, Gd^{3+} cations are particularly employed. Indeed, gadolinium possesses excellent paramagnetic properties highly valuable for MRI as well as X-ray absorption capacities useful for CT in relation to its significant atomic number ($Z = 64$).[11] In 2014, we proposed to use NPs based on gadolinium oxysulfide ($Gd_2O_2S:Eu^{3+}$ and $Gd_2O_2S:Er^{3+},Yb^{3+}$) for trimodal imaging using T_2-weighted MRI, CT and OI.[12] Furthermore, this type of lanthanide-doped Gd_2O_2S NP has been used for mesenchymal stem cell labelling, tracking, and UC bioimaging,[13–15] showing great promise for bio-applications. However, the nanoparticles were synthesized through a complicated solid state sintering method, resulting in a large size (>80 nm) which led to the NPs being metabolized and eliminated by the hepatobiliary system in several months in our recent study.[15] Small (≤20 nm) or even ultrasmall sized NPs (≤10 nm) with good water dispersity could overcome these drawbacks. Thanks to pioneering works[16,17] on the synthesis of rare earth oxysulfide (RE_2O_2S) in the presence of high boiling temperature organic solvents, smaller (5–40 nm) NPs have been prepared. However, a reproducible and general synthesis route for RE_2O_2S NPs with good dispersity, uniform size, and steady reaction yield is still very much needed.[18,19] Besides, the absence of further investigation of surface modification of these as-prepared RE_2O_2S NPs limits their applications in the field of nanomedicine.

In this work, we present a versatile strategy to synthesize 15 kinds of RE_2O_2S NPs with excellent monodispersity and small sizes. Furthermore, we have selected Nd-doped Gd_2O_2S NPs in particular to carry out full investigations for the following reasons: if gadolinium provides contrasting properties already well known in MRI, neodymium has the double advantage of offering intense emission in the second window of biological transparency as well as the highest absorption coefficient of all lanthanides in the NIR area (700–900 nm range),[20] thus enabling detection by photoacoustic imaging. On the basis of transmission electron microscopy (TEM), X-ray diffraction (XRD) and spectroscopy characterization, we investigated the effects of size and doping concentration on the NIR-II down-shifting luminescence intensity of Nd-doped Gd_2O_2S NPs. A ligand exchange method was used to render the $Gd_{0.8}Nd_{1.2}O_2S$ NPs hydrophilic by replacing surface oleic acid with polyvinylpyrrolidone (PVP) molecules. These PVP-coated $Gd_{0.8}Nd_{1.2}O_2S$ NPs displayed good colloidal stability in culture medium and low cytotoxicity on human cells. These NPs were finally proven to be capable of being employed in five types of imaging configurations: NIR-II luminescence, PA, US, MR, and CT. These results are a major step towards *in vivo* multimodal bioimaging using ultrasmall RE_2O_2S NPs as contrast agents.

Experimental

Materials

N,*N*′-Diphenylthiourea (DPTU), $LiOH{\cdot}H_2O$, acetic acid, ethanol, methanol, chloroform, cyclohexane, KBr powder, and PVP (M_W = 10 000) were purchased from Sigma-Aldrich. Oleic acid (OA), oleylamine (OM) and tri-*n*-octylamine (TOA) were purchased from TCI. Milli Q water (18.2 MΩ cm, 25 °C) was produced by the purification system. All rare earth oxides (RE_2O_3, RE = Y, La, Ce, Pr, Nd, Sm, Eu, Gd, Tb, Dy, Ho, Er, Tm, Yb, and Lu) were purchased from Rhône Poulenc. $RE(CH_3COO)_3{\cdot}4H_2O$ was prepared by first dissolving a moderate amount of RE_2O_3 in excess acetic acid solution at 90 °C, then filtering and evaporating the solution, and finally drying the resultant slurry in an oven at 70 °C. All chemicals were used as received without further purification.

Synthesis of ultrasmall RE_2O_2S NPs

RE_2O_2S NPs were prepared through a thermal decomposition method. In a typical synthesis, 1 mmol of $RE(CH_3COO)_3{\cdot}4H_2O$, 1 mmol of $LiOH{\cdot}H_2O$, 3 mL of OA, 7 mL of OM and 10 mL of TOA were mixed in a 100 mL three-necked round-bottom flask and heated to 160 °C under an argon flow with constant stirring for 30 min to form a clear solution. After cooling to room temperature, an ethanol solution (10 mL) of DPTU (3 mmol) was added dropwise and stirred for 30 min. The reaction mixture was then heated to 70 °C and maintained for 60 min to remove the ethanol. After ethanol was evaporated, the resulting solution was heated to 320 °C under an argon flow with vigorous stirring for 60 min, and then cooled down to room temperature (RT). The resulting NPs were collected by centrifugation (5000 rpm, 10 min) by mixing with ethanol, and washed 3 times with both cyclohexane and ethanol. Note that all RE_2O_2S (RE = Y, La, Ce, Pr, Nd, Sm, Eu, Gd, Tb, Dy, Ho, Er, Tm, Yb, and Lu) including Nd-doped Gd_2O_2S NPs were synthesized under the above-described conditions. For optimizing the reaction conditions, solvent ratio, and the amount of DPTU, reaction temperatures and times were varied as described in the Results and discussion section.

Synthesis of PVP-coated $Gd_{0.8}Nd_{1.2}O_2S$ NPs through ligand exchange

The ligand exchange method was adapted from a previously reported protocol[21] with slight modifications. First, 10 mg of NPs were first dispersed in 20 mL of chloroform. After 5 min of constant stirring leading to a transparent suspension, 10 mL of chloroform containing 0.25 g PVP was added. Then the mixture solution was stirred for 72 h at room temperature. PVP-coated $Gd_{0.8}Nd_{1.2}O_2S$ NPs were precipitated by the addition of 30 mL of cyclohexane and collected by centrifugation at 5000 rpm for 15 min. The obtained powder was washed with chloroform and

 This journal is © The Royal Society of Chemistry and the Chinese Chemical Society 2023

Open Access Article. Published on 03 2023. Downloaded on 8/25/2025 2:35:29 AM. This article is licensed under a Creative Commons Attribution-NonCommercial 3.0 Unported Licence.

cyclohexane mixture (1 : 1, V/V) solution twice, and further washed with Milli Q water twice. The purified powder was re-dispersed in water. After that, the suspension was sonicated for another 30 min to obtain a transparent solution, and finally stored at ~4 °C.

Cytotoxicity assay

Primary human dermal fibroblasts were isolated from 4-year old foreskin biopsy commercially available (Icelltis, France). Human HCT-116 colorectal cancer cells (CCL-247) were purchased from ATCC. These cell types were grown in DMEM containing 4.5 g L^{-1} glucose, GLUTAMax, and supplemented with 10% heat-inactivated fetal bovine serum, 100 U mL^{-1} penicillin, and 100 μg mL^{-1} streptomycin. Primary human umbilical vein endothelial cells (HUVEC) were purchased from Angioproteomie and grown in the endothelial growth-2 (EGM-2) medium (Lonza). The cells were maintained at 37 °C under a humidified atmosphere containing 5% CO_2. Throughout the experiments, cells tested negative for mycoplasma (MycoAlert mycoplasma detection kit, Lonza). The day before the experiments, 20 000 HCT-116 cells, or 5000 dermal fibroblasts, or 10 000 HUVECs were seeded in 96 well plates. On the day of the experiment, the cells were incubated for 48 h at 37 °C with increasing concentrations of PVP-coated $Gd_{0.8}Nd_{1.2}O_2S$ nanoparticles, from 0 mg mL^{-1} to 0.1 mg mL^{-1}. Cell viability was then assessed using the PrestoBlue reagent (Invitrogen) according to the manufacturer's instructions. In brief, after 48 h of incubation, the cell culture medium was removed and cells were incubated for 30 min at 37 °C with 100 μL of 1X PrestoBlue reagent diluted in PBS before reading fluorescence at 560/590 nm on a plate reader (Synergy H1, Biotek, Winooski, VT, USA). Six biological replicates were produced and analysed for each condition. A positive control, namely incubation with 75 μg mL^{-1} saponin known to induce cell death, was added to the experiment. Data analysis was performed using GraphPad Prism 8 (GraphPad Software, Inc., La Jolla, CA, USA), and data were expressed as mean ± SEM. Statistical comparisons were performed using one-way analysis of variance (ANOVA), followed by Dunnett's post-test in comparison to the control condition (0 mg mL^{-1}). $*p < 0.05$, $**p < 0.01$, $***p < 0.001$, and $****p < 0.0001$.

Characterization

Nanocrystal size and shape characterization of the RE_2O_2S NPs was performed using a transmission electron microscope (TEM, Phillips CM20 200 kV). The power X-ray diffraction (XRD) patterns were recorded on a Bruker D8 Advance X-ray diffractometer (Cu Kα radiation, λ = 1.5418 Å) with a 2θ range from 20° to 80° at a scanning rate of 1° per minute. NIR-II luminescence spectra were recorded using a spectrometer (Princeton Instruments SpectraPro HRS 500) and an N_2-cooled InGaAs infrared detector (Princeton Instruments PyLoN-JR-1.7) using continuous-wave 808 nm laser excitation (SpectraPhysics Tsunami Ti:Sapphire oscillator). Dynamic light scattering (DLS) was performed on a Malvern Zetasizer to determine the hydrodynamic sizes and size distributions. Fourier transform infrared (FTIR) spectra were recorded on a PerkinElmer Spectrum 100 FTIR spectrometer and the samples were prepared by mixing with KBr fine powder in a pellet. Magnetic measurements were carried out on a MPMS5 Squid magnetometer from Quantum design. For ZFC/FC, the sample was cooled to 2 K prior to application in the field and temperature scanning. For magnetization hysteresis loops, the field was cycled between -5 T and 5 T at either 2 K or 300 K. Longitudinal (T_1) and transverse (T_2) relaxation times of different Gd concentrations were measured on an NMR relaxometer (Bruker Minispec 20 MHz, 37 °C) under a magnetic field of 0.47 T. To carry out multimodal imaging experiments, the PVP-coated $Gd_{0.8}Nd_{1.2}O_2S$ NPs with 3 different series of concentrations (Ser. 1 from 0 to 1.1 mg mL^{-1}, Ser. 2 from 0 to 27.0 mg mL^{-1}, and Ser. 3 from 0 to 30.1 mg mL^{-1}) were dispersed in 10 wt% gelatin phantoms in centrifugal tubes. MRI experiments were performed on a BRUKER pharmascan 70/16 system (BRUKER Biospin, Ettlingen, Germany) equipped with a 7-Tesla magnet and 16 cm horizontal bore size. A transmit–receive volume coil with 40 mm inner diameter was used for all MRI acquisitions. MRI relaxometry methods were performed to estimate T_1 and T_2 at 7 T, procedures are reported in the ESI.† X-Ray tomography scan was carried out on a GERT16 and set from 80 to 140 kV using sample Ser. 2. US (21 MHz) and PA (680–970 nm) experiments were performed simultaneously using an imaging platform dedicated to small animals (Vevo LAZR-X, Visualsonics) (see details in the ESI†) using sample Ser. 3. NIR-II imaging experiments were carried out on a small animal imaging system (Series III 900/1700, NIROPTICS) equipped with a cooled InGaAs camera (900–1700 nm) using the $Gd_{0.8}Nd_{1.2}O_2S$ NPs powder. 1% intralipid medium was used to simulate *in vivo* conditions.

Results and discussion

Synthesis and characterization of ultrasmall RE_2O_2S NPs

Ultrasmall Gd_2O_2S NPs were synthesized through a new high-temperature decomposition method in the presence of OA, OM and TOA as surfactants, DPTU as the sulphur (S) source, and LiOH as the mineralizer (Fig. 1a), where DPTU was for the first time used in the synthesis of RE_2O_2S. The as-synthesized NPs are hydrophobic and can be stably dispersed in various non-polar organic solvents, for instance, cyclohexane.

The Gd_2O_2S crystal has a trigonal structure ($P\bar{3}m1$ space group) with Gd^{3+} ions surrounded by four O^{2-} ions and three S^{2-} ions that form a seven coordinated geometry (Fig. 1b). All Gd^{3+} ions occupy a 2d site with a symmetry of C_{3v}.[22] Powder XRD patterns (Fig. 1c) show a set of indexed diffraction peaks of hexagonal phase Gd_2O_2S (JCPDS no. 00-026-1422) without the impurity phase. The intense and broad peaks are evidence of good crystallinity and small size of the NPs. The typical TEM image (Fig. 1d) shows that the NPs are nanoplates with a mean size of 5.9 ± 0.8 nm in diameter (Fig. S1, ESI†). The high crystallinity of the NPs was further confirmed by measuring the d-spacings of 0.295 nm, 0.198 nm, and 0.185 nm from HRTEM images (Fig. 1e and g) which are related to the (101), (110), and (111) planes of Gd_2O_2S, respectively. Additionally, the corresponding fast Fourier transform (FFT) exhibits a series of clear

Open Access Article. Published on 03 2023. Downloaded on 8/25/2025 2:35:29 AM.
This article is licensed under a Creative Commons Attribution-NonCommercial 3.0 Unported Licence.

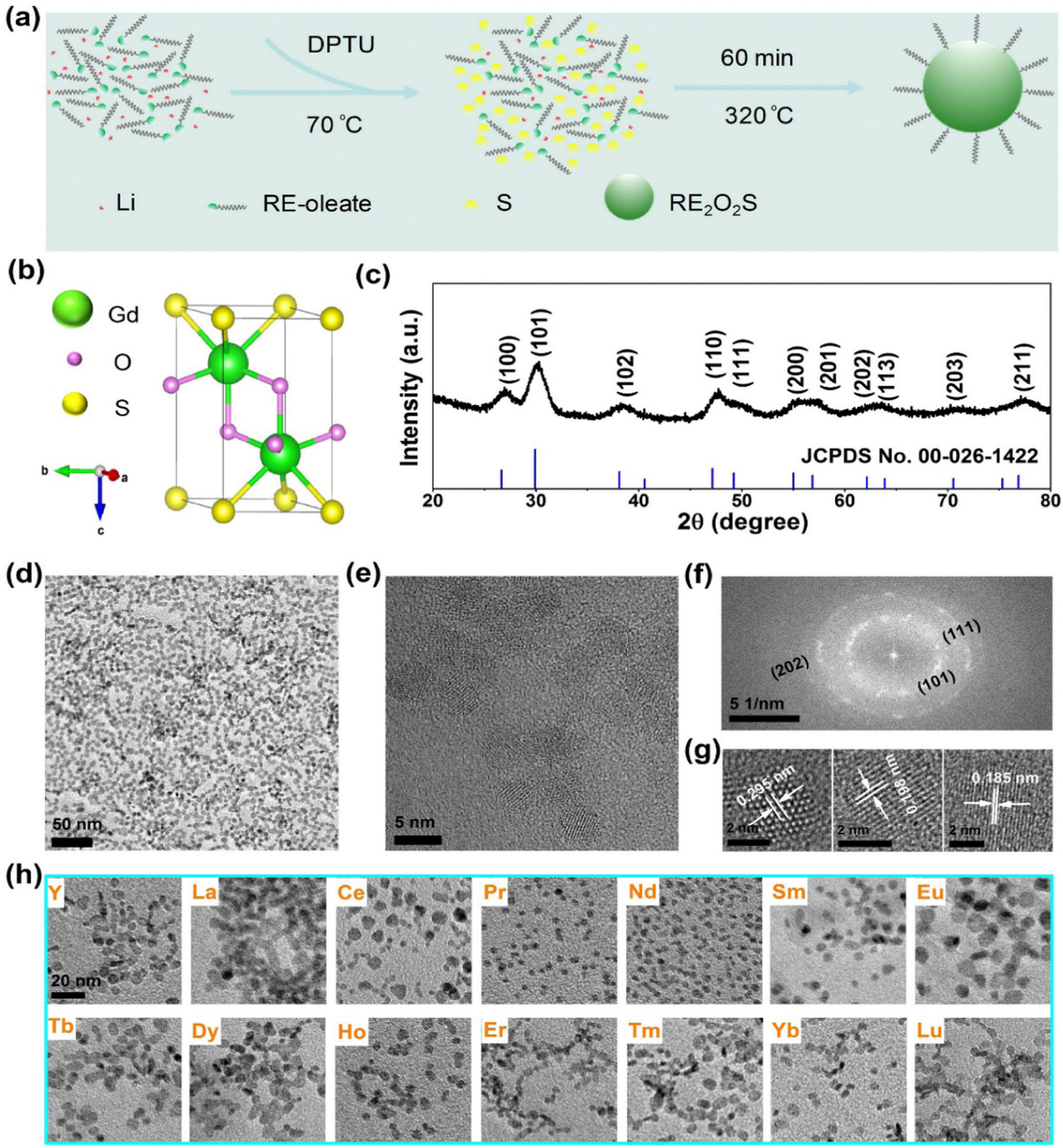

Fig. 1 Characterization of RE_2O_2S NPs. (a) Schematic illustration of the synthesis of RE_2O_2S NPs. (b) VESTA presentation of the crystal structure of hexagonal Gd_2O_2S. (c–g) XRD patterns, typical TEM image, HRTEM image, FFT diffraction and identical planes of Gd_2O_2S NPs, respectively. (h) TEM images of 14 kinds of ultrasmall RE_2O_2S NPs synthesized by the optimized approach.

diffraction rings which can be indexed to the (101), (111), and (202) planes (Fig. 1f).

In previous synthesis of RE_2O_2S NPs based on thermal decomposition of precursors in organic medium, element S_8 powder was reported to be the common sulphur source whereas some other S containing molecules like $Ln[(phen)(ddtc)_3]$ (phen = 1,10-phenanthroline; ddtc = diethyldithiocarbamate) were less used because of their sophisticated preparations. Despite that, it still remains challenging to synthesize nanoscale RE_2O_2S NPs with heavy lanthanides[18] and steady reaction yield.[19] DPTU, reported in other syntheses of metal sulfides, such as CaS,[23,24] has been used in our synthesis and can *in situ* release H_2S at elevated temperatures.

To achieve monodispersed Gd_2O_2S NPs, a range of synthesis parameters were optimized, in which the effect of DPTU was first studied. TEM images (Fig. S2a, ESI†) and XRD patterns

 This journal is © The Royal Society of Chemistry and the Chinese Chemical Society 2023

Open Access Article. Published on 03 2023. Downloaded on 8/25/2025 2:35:29 AM. This article is licensed under a Creative Commons Attribution-NonCommercial 3.0 Unported Licence.

(Fig. S2b, ESI†) show the influence of DPTU on the change of size, morphology, and phase in the syntheses. It was found that Gd_2O_3 impurities or mixtures were present due to low substitution of sulphur for oxygen; however, higher concentrations (more than 3 mmol) of DPTU caused smaller size and poor dispersity maybe because of high concentrations of H_2S released from DPTU. Eventually, 3 mmol of DPTU in the synthesis was optimal.

Solvents can affect the dispersity, morphology, and crystallinity of NPs. As shown in Fig. S3 (ESI†), the influence of various volume ratios of solvents was studied. We observed severe aggregation when using 2 mL of OA, which is probably due to strong interaction between oleate with close distance in the nucleation and growth stages. The volume of OA was thus fixed to 3 mL and the volume of OM was gradually increased from 3 to 7 mL, the TEM images show that the uniformity and dispersity of the NPs were both improved. Unfortunately, the size of the NPs cannot be tuned by adjusting the solvent ratios even if the volume of OA was varied from 2 to 5 mL. Besides, amorphous matter was observed from the XRD pattern in Fig. S4 (ESI†) when 7 mL of OA was used, which is possibly due to the too great distance between oleates for nucleation.

Reaction time and temperature can generally influence the size or morphology of the NPs. By adjusting the reaction time and temperature, we obtained a narrow size distribution of Gd_2O_2S NPs from approximately 5 to 7 nm (Fig. S5, ESI†). Besides, it was found that LiOH plays a very significant role in the synthesis. For example, nothing can be obtained without the addition of LiOH and replacement by NaOH can cause aggregations and unknown phases. Observation of the essential addition of alkaline ions is consistent with previous works.[16,19,25,26] However, there are controversial points on the effects of alkali in this respect and further investigations would be necessary, but they are beyond the scope of this article.

Furthermore, it is essential to investigate the syntheses of other rare earth oxysulfide NPs because of their high performance as luminescent materials for many promising applications. Then, the optimal conditions for the synthesis of Gd_2O_2S were simply applied to that of other RE_2O_2S NPs. Strikingly, we obtained the other 14 kinds of RE_2O_2S (RE = Y, La, Ce, Pr, Nd, Sm, Eu, Tb, Dy, Ho, Er, Tm, Yb, and Lu) NPs (Fig. 1g and Fig. S6, ESI†) with good dispersity and high crystallinity, and the mean sizes ranged from ~3 to ~10 nm (Table S1, ESI†). All the corresponding XRD patterns of the RE_2O_2S NPs can be well indexed to their standard diffraction data (Fig. S7, ESI†). It is worth emphasizing that not only were heavy lanthanide oxysulfides (crystallized and nanoscaled Tm_2O_2S synthesized for the first time, to the best of our knowledge) readily prepared but also a high and steady reaction yield (over 70%) for all RE_2O_2S NPs was roughly estimated, considering 30% of oleates in the final products (according to the previous thermogravimetric analysis of Ln_2O_2S by Carenco's group[27]). These results demonstrate a versatile strategy for the syntheses of ultrasmall RE_2O_2S NPs, which may lead to more investigations of their optical and magnetic properties at such a nanoscale.

NIR-II luminescence of Nd-doped Gd_2O_2S NPs

To obtain ultrasmall RE_2O_2S nanoparticles with efficient NIR-II emission and magnetic properties, we synthesized a series of NIR-II luminescent Nd-doped Gd_2O_2S NPs with different Nd concentrations. As shown in Fig. S8 (ESI†), TEM images show the change of the size and morphology of NPs with varying Nd concentrations. It is observed that the morphology is slightly changed but the size varies in the range of 3–6 nm (Table S1, ESI†). The diffraction peaks of NPs shift to lower diffraction angles with the increase of the Nd concentration (Fig. S9, ESI†), indicating the substitution of larger Nd^{3+} for smaller Gd^{3+}. Under 808 nm laser irradiation, the typical downshifting emission bands of Nd^{3+} at 900, 1078, and 1365 nm were recorded, as shown in Fig. 2. The three main emission peaks can be exclusively assigned to the transitions of $^4F_{3/2} \rightarrow {}^4I_{9/2}$, $^4F_{3/2} \rightarrow {}^4I_{11/2}$, and $^4F_{3/2} \rightarrow {}^4I_{13/2}$ of Nd^{3+}. The integrated downshifting luminescence intensity of Nd^{3+} first decreases and then increases with Nd concentration varying from 10% to 100%. Then the Nd concentration is optimized at 60% (the chemical composition denoted by $Gd_{0.8}Nd_{1.2}O_2S$) by overall consideration of concentration and surface quenching, and size variation.

Surface modification

For the sake of bioimaging application, we synthesized PVP-coated $Gd_{0.8}Nd_{1.2}O_2S$ NPs through a ligand exchange method, as shown in Fig. 3a. Fig. 3b and Fig. S10a (ESI†) show individual OA-coated $Gd_{0.8}Nd_{1.2}O_2S$ NPs with a mean size of 6.0 ± 0.8 nm. After ligand exchange, the as-prepared PVP-coated $Gd_{0.8}Nd_{1.2}O_2S$ NPs displayed excellent water solubility without any visible aggregation and the size was calculated to be 5.9 ± 0.8 nm by TEM observation (Fig. 3c and Fig. S10b, ESI†).

The successful surface functionalization was verified by FTIR spectra, as shown in Fig. 3d. For the spectrum of OA-coated $Gd_{0.8}Nd_{1.2}O_2S$ NPs, the peaks at 1509 cm^{-1} and 1427 cm^{-1} were ascribed to the asymmetric and symmetric

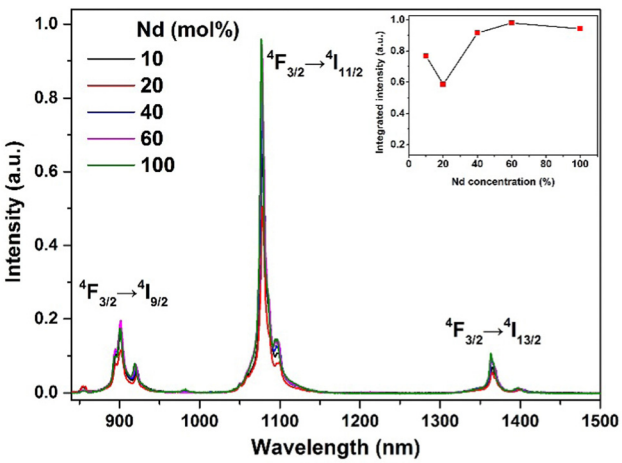

Fig. 2 NIR-II luminescence properties. NIR-II luminescence spectra of a series of Nd-doped Gd_2O_2S NPs under 808 nm continuous wave excitation. The concentration of all suspensions is 20 mg mL^{-1}.

Open Access Article. Published on 03 2023. Downloaded on 8/25/2025 2:35:29 AM.
This article is licensed under a Creative Commons Attribution-NonCommercial 3.0 Unported Licence.

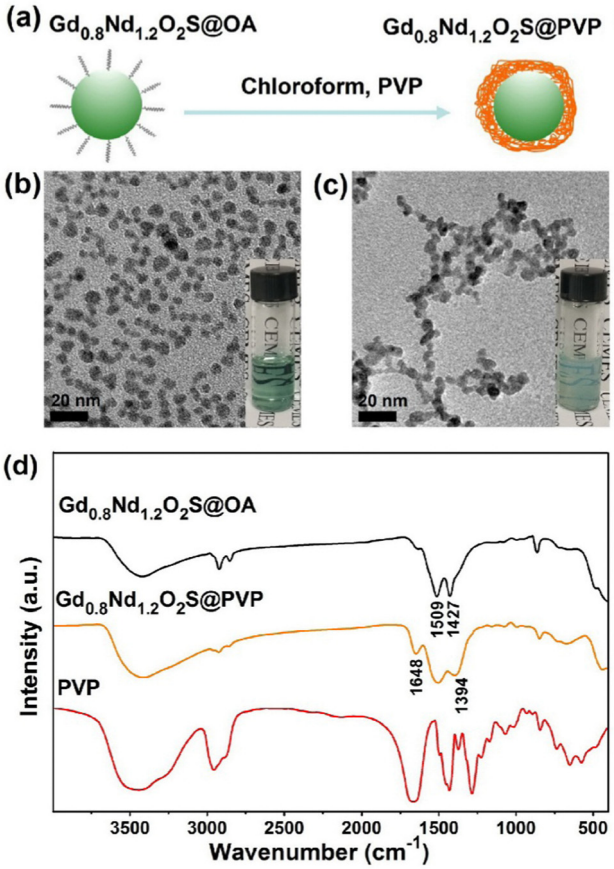

Fig. 3 Ligand exchange with PVP. (a) Schematic illustration of the synthesis of PVP-coated $Gd_{0.8}Nd_{1.2}O_2S$ NPs. (b and c) TEM images of OA-coated and PVP-coated $Gd_{0.8}Nd_{1.2}O_2S$ NPs. Inset photos show the dispersity of nanoparticles in cyclohexane and water with the same concentration of 10 mg mL^{-1}, corresponding to before and after ligand exchange, respectively. (d) FTIR spectra of OA-coated, PVP-coated $Gd_{0.8}Nd_{1.2}O_2S$ NPs and PVP.

stretching vibrations of the COO^- group. After PVP exchange, two peaks at 1648 cm^{-1} and 1394 cm^{-1} appeared, corresponding to the stretching vibrations of C=O and C–N from the PVP, respectively. As expected, the carbonyl band shifts to lower wavenumbers going from free PVP to surface-bound PVP. In order to confirm the colloidal stability of the nanoparticles in the serum-supplemented culture medium, we performed dynamic light scattering measurements right after mixing and after standing at room temperature for 24 h. The number-weighted mean hydrodynamic diameter was found to be virtually identical at 6.8 and 6.4 nm (Fig. S11a, ESI†) and so were the correlograms (Fig. S11b, ESI†).

Cytotoxicity assessment

We further assessed the cytotoxicity of PVP-coated $Gd_{0.8}Nd_{1.2}O_2S$ NPs *in vitro* either on human HCT-116 colorectal cancer cells or on normal primary human cells, namely dermal fibroblasts and human umbilical vein endothelial cells (HUVEC), using the Prestoblue assay. As shown in Fig. 4, the cell viability of tumour HCT-116 and normal dermal fibroblasts was statistically reduced, even at lowest concentrations of PVP-coated $Gd_{0.8}Nd_{1.2}O_2S$ NPs for 48 h. While the viability of cancer cells was 60% at the lowest 0.0001 mg mL^{-1}, the viability of healthy dermal cells was 78%, which highlights the greater sensitivity of cancer cells to PVP-coated $Gd_{0.8}Nd_{1.2}O_2S$ NPs. Interestingly, endothelial cells lining the blood vessels, thus the first cells to be in contact with NPs following their injection into the blood, were not affected by the concentrations tested. These results obviously exhibited low cytotoxicity for normal cells together with a pronounced cytotoxicity against tumour cells of PVP-coated $Gd_{0.8}Nd_{1.2}O_2S$ NPs within our experimental concentration range, showing promising bio-applications for the NPs.

MR and CT imaging

We first measured the magnetic properties of $Gd_{0.8}Nd_{1.2}O_2S$ using a Squid magnetometer. Zero field cooling/field cooling (ZFC/FC) sequences revealed no blocking temperature, as is expected for such particles (Fig. S12, ESI†). Even when studying pure ultrasmall Gd_2O_2S, Larquet *et al.*[28] did not detect any blocking temperature. Besides, the FC and ZFC curves of our $Gd_{0.8}Nd_{1.2}O_2S$ sample are virtually identical which indicates the absence of superparamagnetism, and are well fitted by the Curie law. The Curie constant extracted from this fit is $C = 3.89$, which is in good agreement with the calculated value of 3.98 taking into account the composition of our sample (x = 40% Gd, y = 60% Nd, with $C = x \times (\mu_{obs\,Gd}{}^{3+}/2.83)^2 + y \times (\mu_{obs\,Nd}{}^{3+}/2.83)^2$ and $\mu_{obs\,Gd}{}^{3+} = 7.9$ and $\mu_{obs\,Nd}{}^{3+} = 3.4$).

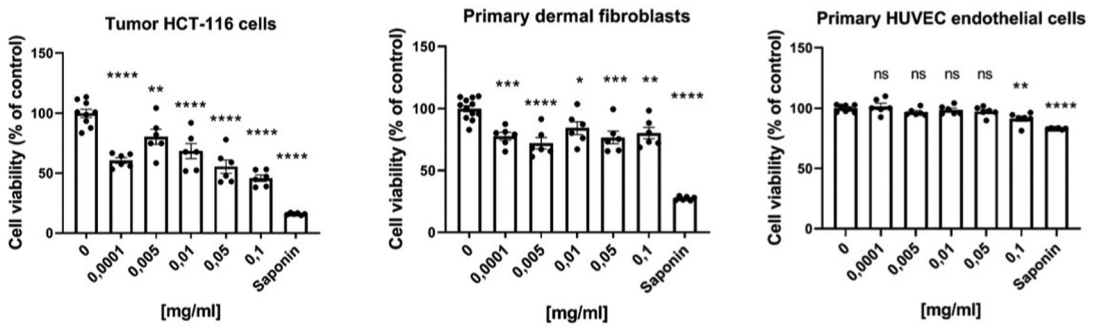

Fig. 4 Cell viability study. Viability of tumour (HCT-116) and normal (dermal fibroblasts, HUVEC) human cells after 48 h incubation with PVP-coated $Gd_{0.8}Nd_{1.2}O_2S$ NPs in the concentration range of 0–0.1 mg mL^{-1}. 75 μg mL^{-1} saponin detergent was used as positive control of cell death.

 This journal is © The Royal Society of Chemistry and the Chinese Chemical Society 2023

Open Access Article. Published on 03 2023. Downloaded on 8/25/2025 2:35:29 AM. This article is licensed under a Creative Commons Attribution-NonCommercial 3.0 Unported Licence.

The magnetization measurements were then carried out at 2 K and 300 K. At 2 K, the sample showed paramagnetic behaviour with a maximum value of M = 81 emu g^{-1} at 5 T (Fig. S13a, ESI†; saturation was not reached and there was no sign of hysteresis). At 300 K, the sample was paramagnetic and the magnetization expectedly dropped to 2.7 emu g^{-1} at 5 T (Fig. S13b, ESI†). At this temperature, the magnetic susceptibility was constant at all field strengths at a value of 8.6×10^{-5} emu g^{-1} Oe^{-1}. This susceptibility compares well with other reported ultrasmall Gd-based nanoparticles such as $NaGdF_4$ (1.049×10^{-4} emu g^{-1} Oe^{-1}).[29]

To validate the potential of PVP-coated $Gd_{0.8}Nd_{1.2}O_2S$ NPs as MR contrast agents, the T_1 and T_2 relaxation times at different Gd concentrations were measured on a relaxometer. Both the T_1 and T_2 relaxation times displayed very linear dependence on the Gd concentration, as shown in Fig. 5a. The longitudinal (r_1) and transversal relaxivity (r_2) values were determined from the slope of the relaxation rate ($1/T$) as a function of Gd^{3+} concentration. As r_1 is related to the change in the relaxation rates of the protons of water in the presence of contrast agents, which requires a high amount of Gd^{3+} ions on the surface and a close distance between water molecules and exterior Gd^{3+} ions to produce a high r_1 value. Luckily, the PVP-coated ultrasmall $Gd_{0.8}Nd_{1.2}O_2S$ NPs have large surface to volume ratios and excellent water dispersibility, exhibiting a r_1 value of 2.42 $(mM)^{-1}$ s^{-1} under a magnetic field of 0.47 T, 37 °C. This value is slightly lower than the r_1 of gadolinium-based clinical agents such as gadopentetate dimeglumine (Gd-DTPA), gadoterate (Gd-DOTA) and gadodiamide (Gd(DTPA-BMA)) in the range of 3.5–3.8 $(mM)^{-1}$ s^{-1} (0.47 T, 37 °C).[30] A quite low r_2 was obtained at 2.83 $(mM)^{-1}$ s^{-1}.

However, images and studies we performed at a stronger magnetic field of 7 T show much more interesting behaviour. Fig. 5b shows T_1- and T_2-weighted MRI of PVP-coated $Gd_{0.8}Nd_{1.2}O_2S$ NPs. With an increase of the NP concentration, the T_1-weighted image becomes brighter; in contrast, T_2-weighted image becomes darker. A high sensitivity of 0.2 mg mL^{-1} was obtained from the images. The r_1 of 9 $(mM)^{-1}$ s^{-1} and r_2 of 57 $(mM)^{-1}$ s^{-1} at 7 T (Fig. S14, ESI†) were further determined by linearly fitting the relaxation rate values extracted from Fig. 5b. The r_2 is relatively close to the transversal relaxivity observed for commercial T_2 contrast agents such as RESOVIST or FERRIDEX (between 100 to 200 $(mM)^{-1}$ s^{-1} depending on conditions). Compared with the highest records of pure Gd based NPs (78.2 $(mM)^{-1}$ s^{-1} for 3 nm $NaGdF_4$[31] and 53.9 $(mM)^{-1}$ s^{-1} for 3–5 nm Gd_2O_3[32]), our $Gd_{0.8}Nd_{1.2}O_2S$ NPs still exhibit a modest r_1 value when taking into account its high Nd doping concentration which decreases the surface Gd^{3+} ion concentrations.

In order to investigate the CT imaging of PVP-coated $Gd_{0.8}Nd_{1.2}O_2S$ NPs, 10 samples were prepared in the centrifuge tubes, the upper layer contained NPs and pure gelatin solution was on the bottom layer as a control. Under X-ray irradiation, the NPs can produce radiation–matter interactions such as

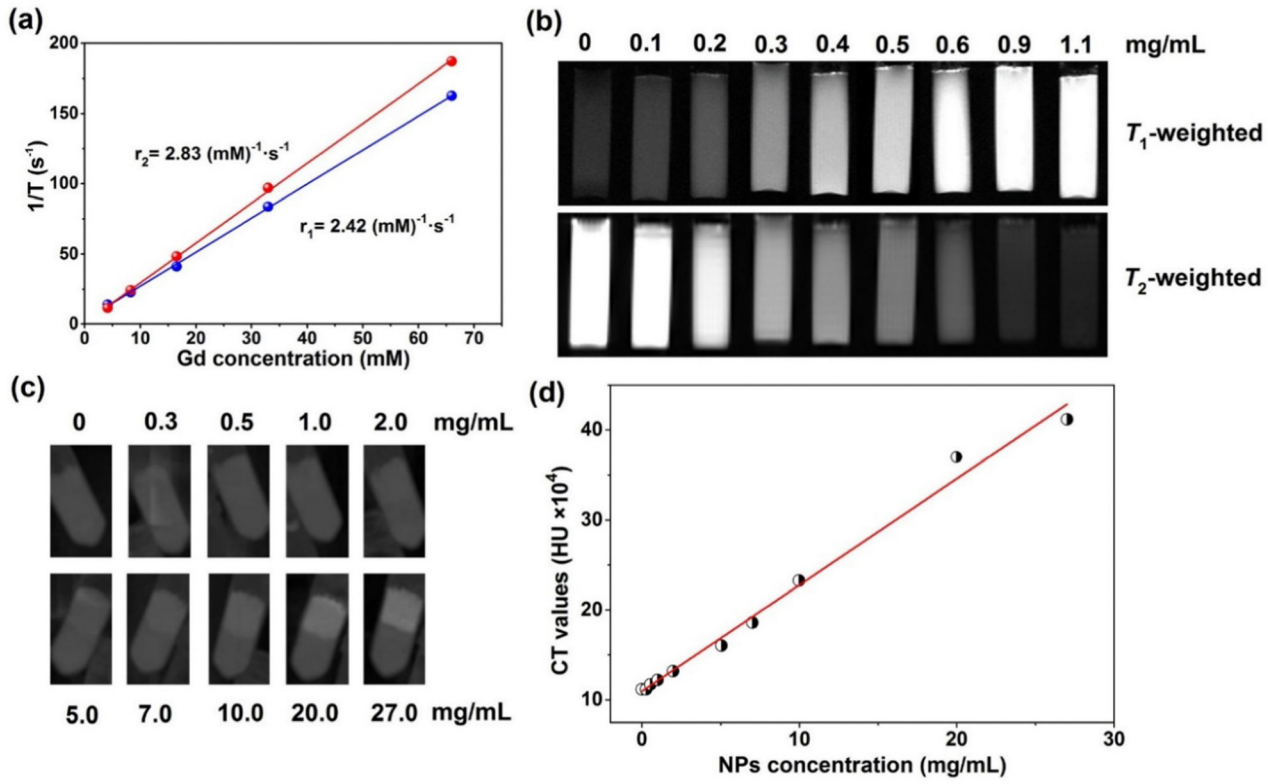

Fig. 5 MR and CT imaging. (a) T_1 and T2 relaxivity plots of the aqueous suspension of PVP-coated $Gd_{0.8}Nd_{1.2}O_2S$ NPs at 0.47 T. (b) T_1- and T2-weighted MRI of PVP-coated $Gd_{0.8}Nd_{1.2}O_2S$ NPs at 7 T for increasing concentration of NPs from 0 to 1.1 mg mL^{-1}. (c) CT imaging intensity variation with increasing concentration of PVP-coated $Gd_{0.8}Nd_{1.2}O_2S$ NPs from 0 to 27 mg mL^{-1}. (d) Plot of HU as a function of NPs concentration.

Open Access Article. Published on 03 2023. Downloaded on 8/25/2025 2:35:29 AM.
This article is licensed under a Creative Commons Attribution-NonCommercial 3.0 Unported Licence.

absorption and Compton scattering, resulting in contrast. Fig. 5c shows that the CT value increases as the concentration of the NPs increases. In other words, X-ray absorption increases with increasing NP concentration. We can clearly see that the contrast starts on the image from the concentration of 2 mg mL^{-1}, then increases with increasing NP concentration. Furthermore, the mean Hounsfield Unit (HU) was collected from the CT image as a function of NP concentration (Fig. 5d). The obtained scattering data show a linear relationship between the CT values and the NP concentrations.

PA, US and NIR-II luminescence imaging

PA and US imaging are presented together because they were performed on the same device from the same batch of samples. Prior to the analyses, we obtained the absorbance spectrum of the $Gd_{0.8}Nd_{1.2}O_2S$ nanoparticles (Fig. S15, ESI†) and found the characteristic bands of Nd^{3+}: from $^4I_{9/2}$ (ground level) to $^4G_{5/2}$ + $^2G_{7/2}$ at 600 nm, to $^4F_{7/2}$ + $^4S_{3/2}$ at 750 nm, to $^4F_{5/2}$ + $^2H_{9/2}$ at 808 nm, and to $^4F_{3/2}$ at around 900 nm. We then performed a scan of the photoacoustic intensity as a function of laser wavelength and found an almost exact match of the excitation bands (Fig. S16, ESI†). The linearity curves of PA and US intensity as a function of the NP concentration are presented in Fig. 6a and b. The sensitivity according to these two imaging techniques seems substantially equivalent and of the same order of magnitude as for the tomodensitometry. A comparison of PA and US images recorded for concentrations of 0 and 30 mg mL^{-1} under an excitation of 685 nm clearly highlighted the enhanced signals from the NPs existing area down to 5–7 mm depth (Fig. 6c). Although this concentration range is beyond the clinically reasonable range, it helped establish the feasibility of the detection by these two modalities.

To explore the potential of bioimaging at the NIR-II biological window, we first carried out the study of penetration depth in intralipid medium of $Gd_{0.8}Nd_{1.2}O_2S$ NPs under 808 nm laser excitation (50 mW cm^{-2}) using a small animal imaging system, as shown in Fig. 6d. The as-prepared NPs were covered with a Petri dish containing the intralipid medium (1%) with varied thicknesses from 0 to 11 mm and the images were taken with 75 ms exposure time. It was observed that although the luminescence intensity drastically decreased as the thickness of the intralipid medium increased, a relevant fluorescence signal still can be collected with a thickness of 11 mm (Fig. 6e). The optical penetration length can be estimated by the following equation:[33,34]

$$I = I_0 \exp(-d/L_p) \quad (1)$$

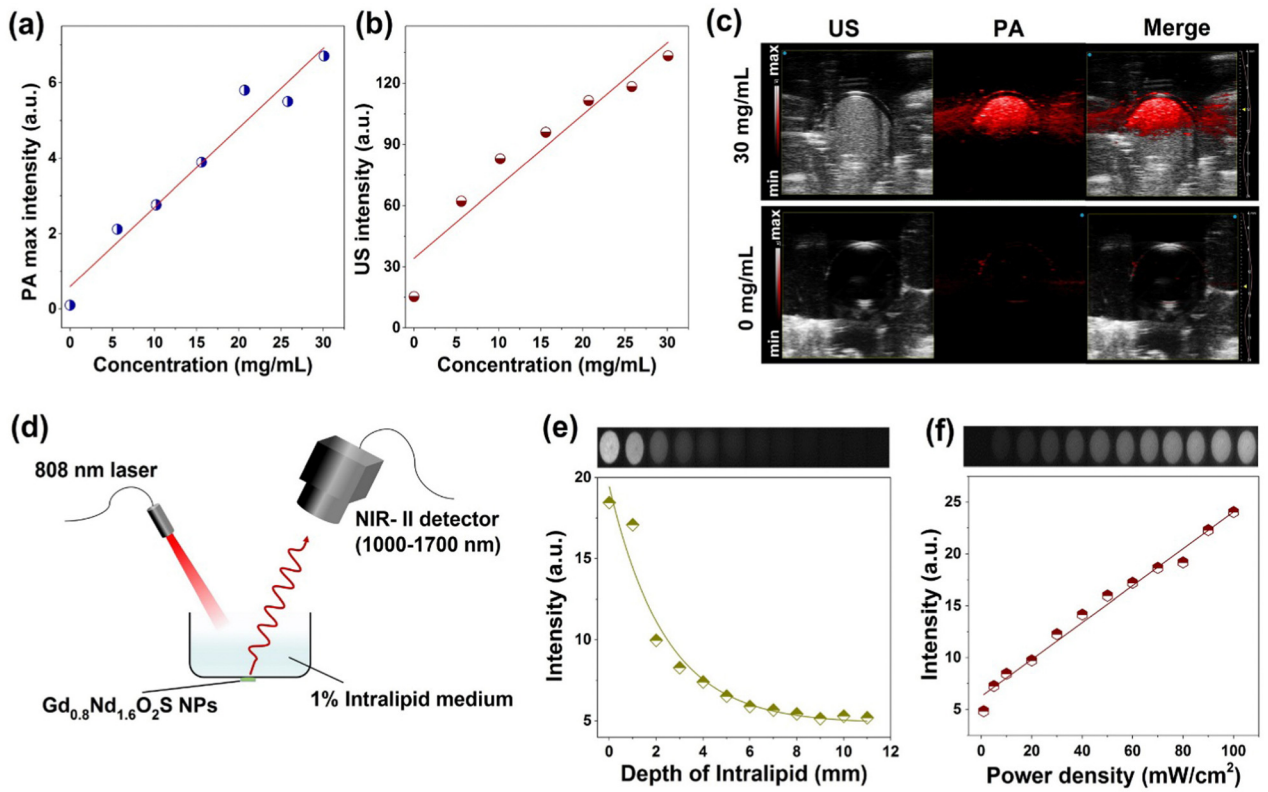

Fig. 6 PA, US, and NIR-II luminescence imaging of $Gd_{0.8}Nd_{1.2}O_2S$ NPs. Plots of (a) PA and (b) US intensities as a function of NP concentration from 0 to 30 mg mL^{-1}. (c) Comparison images obtained under PA, US, and merge channels for NPs at concentrations 0 and 30 mg mL^{-1}. (d) Schematic illustration for NIR-II luminescence imaging of $Gd_{0.8}Nd_{1.2}O_2S$ NPs covered with a 1% intralipid medium. (e) NIR-II luminescence intensities obtained for the NPs with respect to immersion depth of the Intralipid medium under 808 nm laser excitation with a power density of 50 mW cm^{-2}. (f) Plot of intensity as a function of the laser excitation power density with an intralipid depth of 2 mm. Inset photos in (e) and (f) show the variations with the intralipid depth and power density increasing, respectively, and exposure time of 75 ms for all images.

 This journal is © The Royal Society of Chemistry and the Chinese Chemical Society 2023

Open Access Article. Published on 03 2023. Downloaded on 8/25/2025 2:35:29 AM. This article is licensed under a Creative Commons Attribution-NonCommercial 3.0 Unported Licence.

where I is the intensity, I_0 is a constant, d is the depth and L_p is the optical penetration length. The resulting fitting curve matches well with our experimental data and the fitted value of L_p is 2.4 mm. The penetration length is comparable to that of LaF_3:Nd NPs,[35] but lower than that of $LiLuF_4$:Nd@$LiLuF_4$ NPs (20 mm penetration length reported).[36] We further investigated the power-dependent imaging performance of $Gd_{0.8}Nd_{1.2}O_2S$ NPs with a fixed depth (2 mm) of intralipid medium, as shown in Fig. 6f. The inset photo shows that the luminescence intensity gradually increases with elevated excitation power, while the signals can be detected when power density lowers to 5 mW cm^{-2}. The fitting curve shows a linear relationship between luminescence intensity and laser power density. Considering the very small size and the absence of inert shell protection of our $Gd_{0.8}Nd_{1.2}O_2S$ NPs, we strongly believe that it holds great promise for NIR-II bioimaging application.

Conclusions

We have developed a versatile strategy for synthesizing 15 kinds of ultrasmall RE_2O_2S NPs whose sizes range from 3 to 11 nm. Among these NPs, $Gd_{0.8}Nd_{1.2}O_2S$ NPs were demonstrated to be promising contrast agents for MRI, CT, PAI, USI, and NIR-II luminescence imaging. The PVP-coated ultrasmall $Gd_{0.8}Nd_{1.2}O_2S$ NPs were prepared through a ligand exchange method and showed low but variable toxicity in a large range of concentrations assessed depending on the cell line, with the endothelial line being largely unaffected. The r_1 of 2.42 $(mM)^{-1}$ s^{-1} and r_2 of 2.83 $(mM)^{-1}$ s^{-1} were obtained for the PVP-coated $Gd_{0.8}Nd_{1.2}O_2S$ NPs. However, T_1- and T_2-weighted MRI under a higher magnetic field (7 T) gave higher r_1 of 9 $(mM)^{-1}$ s^{-1} and r_2 of 57 $(mM)^{-1}$ s^{-1} showing the potential of *in vivo* T_1- and T_2-weighted bimodal MRI which allows differentiation of signals induced by T_2 contrast agents from a low-level background. PAI, USI and CT showed equivalent sensitivity in the assessed concentration range. Unsurprisingly, this sensitivity is about 10 times lower than that for MRI (detection limit around a few mg mL^{-1} instead of 0.2 mg mL^{-1}). It is nonetheless interesting because these three techniques are much less expensive and more easily accessible than MRI. Using NIR-II luminescence imaging technique, the optical penetration length of 2.4 mm was determined at a power density of 50 mW cm^{-2}. All of these findings thus pave the way, not only for preparation of ultrasmall water-soluble RE_2O_2S NPs, but also for future application of *in vivo* multimodal bioimaging.

Author contributions

QZ: conceptualization, investigation, and writing – original draft; LP: investigation; LG: investigation; DL: investigation; JH: investigation; HZ: supervision and funding acquisition; FD: investigation and funding acquisition; PS: supervision and funding acquisition; NP: investigation; MV: investigation and writing – reviewing and editing; RM: supervision, funding acquisition, writing, and project administration; CR: supervision, writing, and project administration.

Conflicts of interest

There are no conflicts to declare.

Acknowledgements

The authors acknowledge Agence Nationale de la Recherche for funding (ANR-21-CE09-0018), the Natural Science Foundation of China (no. 11804338), Imagerie du Petit Animal de Montpellier (IPAM) for access to high-resolution ultrasound (LRQA Iso9001; France Life Imaging (grant ANR-11-INBS-0006); IBISA; Fondation Leducq (RETP), I-Site Muse). Non-Invasive Exploration service US006 CREFRE Inserm/UPS Laboratory of Toulouse for access to MRI 7 T preclinical unit and Université Toulouse III Paul Sabatier for the PhD scholarship to Q Zou. Dr Cécile Marcelot and Nicolas Ratel-Ramond are acknowledged for performing HR-TEM and XRD measurements. The authors thank Dr Diana Ciuculescu-Pradines for fruitful discussions.

References

1 D. E. J. G. J. Dolmans, D. Fukumura and R. K. Jain, Photodynamic therapy for cancer, *Nat. Rev.*, 2003, **3**, 380–387.
2 R. Weissleder and M. J. Pittet, Imaging in the era of molecular oncology, *Nature*, 2008, **452**, 580–589.
3 M.-K. Tsang, Y.-T. Wong and J. Hao, Cutting-edge nanomaterials for advanced multimodal bioimaging applications, *Small Methods*, 2018, **2**, 1700265.
4 P. Sharma, S. Brown, G. Walter, S. Santra and B. Moudgil, Nanoparticles for bioimaging, *Adv. Colloid Interface Sci.*, 2006, **123–126**, 471–485.
5 A. M. Smith, M. C. Mancini and S. Nie, Bioimaging: second window for in vivo imaging, *Nat. Nanotechnol.*, 2009, **4**, 710–711.
6 K. Welsher, S. P. Sherlock and H. Dai, Deep-tissue anatomical imaging of mice using carbon nanotube fluorophores in the second near-infrared window, *Proc. Natl. Acad. Sci. U. S. A.*, 2011, **108**, 8943–8948.
7 G. Hong, S. Diao, J. Chang, A. L. Antaris, C. Chen, B. Zhang, S. Zhao, D. N. Atochin, P. L. Huang, K. I. Andreasson, C. J. Kuo and H. Dai, Through-skull fluorescence imaging of the brain in a new near-infrared window, *Nat. Photon.*, 2014, **8**, 723–730.
8 S. Diao, G. Hong, A. L. Antaris, J. L. Blackburn, K. Cheng, Z. Cheng and H. Dai, Biological imaging without autofluorescence in the second near-infrared region, *Nano Res.*, 2015, **8**, 3027–3034.
9 J. Xu, A. Gulzar, P. Yang, H. Bi, D. Yang, S. Gai, F. He, J. Lin, B. Xing and D. Jin, Recent advances in near-infrared emitting lanthanide-doped nanoconstructs: Mechanism, design and application for bioimaging, *Coord. Chem. Rev.*, 2019, **381**, 104–134.

Open Access Article. Published on 03 2023. Downloaded on 8/25/2025 2:35:29 AM. This article is licensed under a Creative Commons Attribution-NonCommercial 3.0 Unported Licence.

10 H. David, A. Ughetto, P. Gaudard, M. Plawecki, N. Paiyabhroma, E. Zub, P. Colson, S. Richard, N. Marchi and P. Sicard, Experimental myocardial infarction elicits time-dependent patterns of vascular hypoxia in peripheral organs and in the brain, *Front. Cardiovasc. Med.*, 2021, **7**, 615507.

11 H. Dong, S.-R. Du, X.-Y. Zheng, G.-M. Lyu, L.-D. Sun, L.-D. Li, P.-Z. Zhang, C. Zhang and C.-H. Yan, Lanthanide nanoparticles: From design toward bioimaging and therapy, *Chem. Rev.*, 2015, **115**, 10725–10815.

12 S. A. Osseni, S. Lechevallier, M. Verelst, P. Perriat, J. Dexpert-Ghys, D. Neumeyer, R. Garcia, F. Mayer, K. Djanashvili, J. A. Peters, E. Magdeleine, H. Gros-Dagnac, P. Celsis and R. Mauricot, Gadolinium oxysulfide nanoparticles as multimodal imaging agents for T_2-weighted MR, X-ray tomography and photoluminescence, *Nanoscale*, 2014, **6**, 555–564.

13 J. Santelli, C. Lepoix, S. Lechevallier, C. Martinez, D. Calise, Q. Zou, S. Moyano, D. Cussac, M. Verelst and R. Mauricot, Custom NIR imaging of new up-conversion multimodal gadolinium oxysulfide nanoparticles, *Part. Part. Syst. Charact.*, 2021, **38**, 2000216.

14 J. Santelli, S. Lechevallier, H. Baaziz, M. Vincent, C. Martinez, R. Mauricot, A. Parini, M. Verelst and D. Cussac, Multimodal gadolinium oxysulfide nanoparticles a versatile contrast agent for mesenchymal stem cell labeling, *Nanoscale*, 2018, **10**, 16775–16786.

15 J. Santelli, S. Lechevallier, D. Calise, D. Marsal, A. Siegfriedb, M. Vincent, C. Martinez, D. Cussac, R. Mauricot and M. Verelst, Multimodal gadolinium oxysulfide nanoparticles for bioimaging: A comprehensive biodistribution, elimination and toxicological study, *Acta Biomater.*, 2020, **108**, 261–272.

16 Y. Ding, J. Gu, J. Ke, Y.-W. Zhang and C.-H. Yan, Sodium doping controlled synthesis of monodisperse lanthanide oxysulfide ultrathin nanoplates guided by density functional calculations, *Angew. Chem., Int. Ed.*, 2011, **50**, 12330–12334.

17 F. Zhao, M. Yuan, W. Zhang and S. Gao, Monodisperse lanthanide oxysulfide nanocrystals, *J. Am. Chem. Soc.*, 2006, **128**, 11758–11759.

18 C. Larquet and S. Carenco, Metal oxysulfides: From bulk compounds to nanomaterials, *Front. Chem.*, 2020, **8**, 179.

19 C. Larquet, D. Carriere, A.-M. Nguyen, T. K.-C. Le, X. Frogneux-Plé, I. Génois, P. L. Griel, A. Gauzzi, C. Sanchez and S. Carenco, Unraveling the role of alkali cations in the growth mechanism of Gd_2O_2S nanoparticles, *Chem. Mater.*, 2020, **32**, 1131–1139.

20 M. Runowski, N. Stopikowska and S. Lis, UV-Vis-NIR absorption spectra of lanthanide oxides and fluorides, *Dalton Trans.*, 2020, **49**, 2129–2137.

21 T. Wang, M. Yang, J. Huang, Y. Zhao, H. Wang, S. Leng, J. Chen, G. Sun and J. Liu, NIR-to-NIR UCL/T_1-weighted MR/CT multimodal imaging by $NaYbF_4$:Tm@$NaGdF_4$:Yb-PVP upconversion nanoparticles, *Sci. Bull.*, 2017, **62**, 903–912.

22 I. P. Machado, V. C. Teixeira, C. C. S. Pedroso, H. F. Brito and L. C. V. Rodrigues, X-ray scintillator Gd2O2S:Tb3+ materials obtained by a rapid and cost-effective microwave-assisted solid-state synthesis, *J. Alloys Compd.*, 2019, **777**, 638–645.

23 Y. Gao, R. Li, W. Zheng, X. Shang, M. Zhang, J. Xu, W. You, Z. Chen and X. Chen, Broadband NIR photostimulated luminescence nanoprobes based on CaS:Eu2+,Sm3+ nanocrystals, *Chem. Sci.*, 2019, **10**, 5452–5460.

24 M. Zhang, W. Zheng, P. Huang, Z. Gong, J. Wei, Y. Gao, S. Zhou, X. Li and X. Chen, A new class of blue-LED-excited NIR-II luminescent nanoprobes based on lanthanide-doped CaS nanoparticles, *Angew. Chem., Int. Ed.*, 2019, **58**, 9556–9560.

25 T. Zhang, J. Gu, Y. Ding, Y.-W. Zhang and C.-H. Yan, Experimental and theoretical studies on the controlled synthesis of alkali-metal-doped rare-earth oxysulfide nanocrystals, *ChemPlusChem*, 2013, **78**, 515–521.

26 L. Lei, S. Zhang, H. Xia, Y. Tian, J. Zhang and S. Xua, Controlled synthesis of lanthanide-doped Gd_2O_2S nanocrystals with a novel excitation-dependent multicolor emissions, *Nanoscale*, 2017, **9**, 5718–5724.

27 C. Larquet, D. Hourlier, A.-M. Nguyen, A. Torres-Pardo, A. Gauzzi, C. Sanchez and S. Carenco, Thermal stability of oleate-stabilized Gd_2O_2S nanoplates in inert and oxidizing atmospheres, *ChemNanoMat*, 2019, **5**, 539–546.

28 C. Larquet, Y. Klein, D. Hrabovsky, A. Gauzzi, C. Sanchez and S. Carenco, Tunable magnetic properties of $(Gd,Ce)_2O_2S$ oxysulfide nanoparticles, *Eur. J. Inorg. Chem.*, 2019, 762–765.

29 M.-K. Tsang, S. Zeng, H. L. W. Chan and J. Hao, Surface ligand-mediated phase and upconversion luminescence tuning of multifunctional $NaGdF_4$:Yb/Er materials with paramagnetic and cathodoluminescent characteristics, *Opt. Mater.*, 2013, **35**, 2691–2697.

30 Z. Zhou and Z.-R. Lu, Gadolinium-based contrast agents for magnetic resonance cancer imaging, *Wiley Interdiscip. Rev.: Nanomed. Nanobiotechnol.*, 2013, **5**, 1–18.

31 N. J. J. Johnson, S. He, V. A. Nguyen Huu and A. Almutairi, Compact micellization: A strategy for ultrahigh T_1 magnetic resonance contrast with Gadolinium-based nanocrystals, *ACS Nano*, 2016, **10**, 8299–8307.

32 S. L. Mekuria, T. A. Debele and H.-C. Tsai, Encapsulation of gadolinium oxide nanoparticle (Gd_2O_3) contrasting agents in PAMAM dendrimer templates for enhanced magnetic resonance imaging in vivo, *ACS Appl. Mater. Interfaces*, 2017, **9**, 6782–6795.

33 N.-N. Dong, M. Pedroni, F. Piccinelli, G. Conti, A. Sbarbati, J. E. Ramírez-Hernández, L. M. Maestro, M. d C. I. d l Cruz, F. Sanz-Rodríguez, A. Juarranz, F. Chen, F. Vetrone, J. A. Capobianco, J. G. Solé, M. Bettinelli, D. Jaque and A. Speghini, NIR-to-NIR two-photon excited CaF2: Tm3+,Yb3+ nanoparticles: Multifunctional nanoprobes for highly penetrating fluorescence bio-imaging, *ACS Nano*, 2011, **5**, 866–8671.

34 L. Wu, J. Hu, Q. Zou, Y. Lin, D. Huang, D. Chen, H. Lu and H. Zhu, Synthesis and optical properties of a Y3(Al/Ga)5O12:Ce3+,Cr3+,Nd3+ persistent luminescence nanophosphor: A promising near-infrared-II nanoprobe for biological applications, *Nanoscale*, 2020, **12**, 14180–14187.

35 U. Rocha, K. U. Kumar, C. Jacinto, I. Villa, F. Sanz-Rodríguez, M. d C. I. d l Cruz, A. Juarranz, E. Carrasco,

Open Access Article. Published on 03 2023. Downloaded on 8/25/2025 2:35:29 AM.
This article is licensed under a Creative Commons Attribution-NonCommercial 3.0 Unported Licence.

F. C. J. M. V. Veggel, E. Bovero, J. G. Solé and D. Jaque, Neodymium-doped LaF_3 nanoparticles for fluorescence bioimaging in the second biological window, *Small*, 2014, **10**, 1141–1154.

36 Q.-S. Qin, P.-Z. Zhang, L.-D. Sun, S. Shi, N.-X. Chen, H. Dong, X.-Y. Zheng, L.-M. Li and C.-H. Yan, Ultralow-power near-infrared excited neodymium-doped nanoparticles for long-term in vivo bioimaging, *Nanocale*, 2017, **9**, 4660–4664.